D2.1 Initial Report on Use Cases, integration process flow definition and system/component specifications and designs

Project Information

Project name:	**A Multiplexed plasmo-photonic Biosensing platfoRm fOr rapid and intelligent Sepsis dIAgnosis at the point of care**
Project acronym:	AMBROSIA
Project start date:	1/1/2023
Project duration:	48 months
Contract number:	101093166
Project coordinator:	Nikolaos Pleros / AUTH
Topic:	HORIZON-CL4-2022-DIGITAL-EMERGING-01-03: Advanced multi-sensing systems

Document Information

Document number and title:	D2.1 Initial Report on Use Cases, integration process flow definition and system/component specifications and designs
Document type:	R-Document, report
Contractual date of delivery:	31/08/2023
Calendar date of delivery:	16/10/2023
Work package number:	WP2 System architecture and subsystem conceptual design and specifications
Lead partner:	VHIR
Dissemination level:	PU
Document status:	Version 1

Author List:

Organization	Author
AUTH	Evangelia Chatzianagnostou, Stylianos (Stelios) Simos, Konstantinos Fotiadis, Dimosthenis Spasopoulos
ICN2	M. Carmen Estévez
VHIR	Juan José González-López, Juan Carlos Ruiz Rodríguez
MILQ	Santiago Cocaña del Castillo, Ramakrishna Vasireddi
ARGO	Michal Szaj
SMART	Guilherme Sombrio
XCEL	Alex Farrell
BIOPIX-T	Alexandros Pantazis
SOTON	Frederic Gardes, Thalia Dominguez Bucio, Ioannis Zeimpekis, Xingshi Yu
LGT	José Carreira, Gabriele Navickaite, Michael Geiselmann, Michael Zervas
UB	Jean-Claude Weeber, Aurore Andrieux, Juan-Miguel Arocas Garcia, Kirill Vasilev
UOI	Dimitris Bellas, Eleftheria Lampadariou, Elefterios Lidorikis

TABLE OF CONTENTS

1. Executive summary

This deliverable describes the initial aspects considered for the development of the AMBROSIA prototypes, related to the architecture and conceptual design of the device, and the specification and use cases for the clinical application of sepsis diagnosis. The deliverable includes both clinical specifications (the set of sepsis biomarkers and pathogens selected as more relevant to be detected, the clinical levels for each clinical scenario, and sample requirements and sensing protocols) and technical aspects for the biosensor Point-of-Care platform (related to the design and specifications of the plasmo-photonic and neuromorphic sensor, the microfluidics requirements, the electronics, and other subsystems and interfaces like POC prototype design and software). This deliverable summarizes the initial set of designs and considerations which may be updated with any possible readjustments needed during the development of the biosensing platform.

2. Introduction

2.1. Purpose of this document

The objective of this deliverable is to summarize the panel of biomarkers selected for sepsis diagnosis based on clinical data currently available in the literature which can help in the early diagnosis of sepsis, help in risk stratification and assessing the prognosis of the septic patient and in guiding and monitoring the antibiotic therapy in different sepsis scenarios. We also describe a list of causative pathogens selected for its detection with the proposed platform. Also, at this stage, a set of generic technical system requirements has been specified to develop the Point-of-Care prototype, including the range of concentrations for each biomarker that the system should be able to detect among other general features. Finally, the technical specifications, conceptual designs and integration process flows of all subsystems are described.

2.2. Document structure

The present deliverable is split into the following major parts:

- Use cases and validation scenarios for sepsis diagnosis
- Technical specifications, conceptual designs and integration process flow related to all subsystems of the AMBROSIA PoC diagnostic platform
- Conclusions

2.3. Audience

The content of this document is public.

3. Use cases and validation scenarios for sepsis diagnosis

3.1. Definition of use cases and clinical scenarios

Sepsis is a life-threatening organ dysfunction caused by a dysregulated host response to infection. Sepsis is one of the greatest challenges in hospitals, where it is one of the main causes of death, accounting for 50 million cases worldwide, with almost 20% of reported deaths [1]. Sepsis continues to be an important public health issue and is a leading cause of morbidity and mortality worldwide despite the use of antibiotics and resuscitation therapies [2,3]. The early diagnosis and subsequent stratification of its severity are very important and increase the possibility of starting timely and specific treatments and is crucial to reducing mortality risk [4].

Several definitions and scoring methods have been developed to assist in the identification and rapid diagnosis of sepsis. One widely recognized and extensively utilized scoring system is the Sequential Organ Failure Assessment (SOFA) score, which categorizes the risk of multiple organ failure based on an objective score that includes variables from six organ systems [5,6]. It is primarily used in intensive care units (ICUs) to monitor the progression of organ dysfunction and predict patient outcomes. While the SOFA score is not a standalone diagnostic tool for sepsis, it can be used as part of a comprehensive evaluation. In 2016, the Third International Consensus Conference (Sepsis-3) introduced new criteria for sepsis diagnosis, which include an increase of 2 or more in the SOFA score as one of the diagnostic criteria. This redefinition of sepsis replaced the previously used Systemic Inflammatory Response Syndrome (SIRS)[3,7,8]. The SOFA score is often used in conjunction with other clinical indicators, such as vital signs, laboratory tests, and clinical judgment, to assess the presence and severity of sepsis. It helps healthcare providers stratify the risk of multi-organ failure and predict patient outcomes. Higher SOFA scores in sepsis patients are

associated with increased mortality rates, indicating a more severe disease state and a higher risk of poor outcomes. Overall, while the SOFA score is not specifically designed for sepsis diagnosis, it plays a valuable role in assessing organ dysfunction and guiding the management of sepsis patients, helping healthcare providers make informed decisions about treatment strategies and monitoring patient progress[6,9,10].

Patients with suspected infection who are likely to have a prolonged ICU stay or to die in the hospital can be promptly identified at the bedside with the quick Sequential Organ Failure Assessment (qSOFA). qSOFA is a simplified screening tool used to quickly identify patients at higher risk of poor outcomes due to suspected infection, including sepsis [3]. While SOFA provides a more detailed assessment, qSOFA serves as a rapid bedside evaluation to prompt further evaluation and clinical judgment for sepsis. SOFA evaluates multiple variables from six organ systems, considering specific clinical and laboratory parameters and qSOFA evaluates three clinical criteria - altered mental status, hypotension (systolic blood pressure ≤100 mm Hg), and tachypnea (respiratory rate ≥22/min).

Septic shock is defined as a subset of sepsis in which underlying circulatory and cellular metabolism abnormalities are profound enough to substantially increase mortality. Patients with septic shock can be identified with a clinical construct of sepsis with persisting hypotension requiring vasopressors to maintain MAP ≥65 mm Hg and having a serum lactate level >2 mmol/L (18 mg/dL) despite adequate volume resuscitation. With these criteria, hospital mortality is in excess of 40% [3].

Score systems like qSOFA have been developed to assist in the early identification of sepsis. However, there are concerns regarding the qSOFA sensitivity in detecting sepsis, particularly in identifying patients who are at risk of developing septic shock [8]. This limitation prompted the Surviving Sepsis Campaign, an international initiative aimed at improving sepsis management, to release updated guidelines in 2021. The Surviving Sepsis Campaign guidelines advised against using qSOFA as a standalone screening tool for sepsis. While qSOFA is a simple and easily applicable scoring system, studies have indicated that it may not have sufficient sensitivity in detecting sepsis cases, potentially leading to missed or delayed diagnoses. The guidelines emphasize the need for a more comprehensive approach that combines clinical judgment, vital signs, and laboratory findings to identify sepsis accurately. Blood biomarkers may provide the extra information required to identify this subgroup of patients with high risk, or those who are developing organ failure, despite a low SOFA score.

3.2. Identification of the set of sepsis biomarkers and pathogens

The diagnosis of sepsis is not always straightforward, particularly in critically ill patients who often have complex ongoing disease processes. Many of these patients will also have received antimicrobial therapy that can render microbial cultures negative; several observational studies have reported negative culture results in as many as 30–40% of Intensive Care Unit (ICU) patients with severe sepsis. Even when cultures are positive, results can take several days to become available, thus slowing the diagnostic process and the specific treatment.

The sepsis process is triggered by an invasion of pathogens into the blood stream together with the host response to this invasion [11]. Any other severe insults (burns, trauma, pancreatitis, severe surgery, resuscitated cardiac arrest) can be accompanied by a SIRS. The discrimination of a SIRS with and without infection remains the main problem in the clinical setting. Thus, confirming infection as cause of a severe inflammatory response is the main challenge in the diagnosis of sepsis. To diagnose infection means to find the source of infection, to isolate the causal microorganism and identify its susceptibility to antibiotics. During this process, the innate immune response stimulates macrophages to produce tumor necrosis factor (TNF), interleukin-1, and interleukin-6. These three proinflammatory cytokines produce a

SIRS syndrome which is characteristic of early sepsis. In septic shock, evidence of widespread organ dysfunction is also present, including multi-organ dysfunction, in which patients suffer cardiovascular collapse unresponsive to fluid resuscitation and vasopressor therapy.

The use of sepsis biomarkers has gained attention in the diagnosis and prognosis of sepsis. Over 200 biomarkers have been identified, offering potential utility in the assessment of sepsis. However, it is important to note that not all these biomarkers possess the necessary specificity or sensitivity to be routinely employed in clinical practice. While there is a wide range of biomarkers available, their ability to accurately distinguish sepsis from other inflammatory responses or predict outcomes varies. Some biomarkers may exhibit limited discriminatory power or may not have undergone comprehensive evaluation in diverse clinical conditions. The challenge lies in identifying biomarkers that can reliably indicate the presence of sepsis and provide valuable prognostic information. These biomarkers should be able to differentiate sepsis from non-infectious inflammatory conditions and accurately predict patient outcomes, helping guide treatment decisions. Considering this, during the initial phase of the AMBROSIA project, we have focused on identifying a set of highly significant sepsis biomarkers that can contribute to the following areas: (I) early detection of sepsis in patients displaying systemic inflammatory response syndrome (SIRS); (II) risk stratification and prognosis evaluation of septic patients; and (III) guiding and monitoring antibiotic therapy in various sepsis scenarios. The biomarkers currently envisaged for the AMBROSIA project are C-reactive protein (CRP), procalcitonin (PCT), interleukin-6 (IL-6), the mid-regional fragment of proadrenomedullin (MR-pro-ADM) in addition to the detection of the bacteria *Escherichia coli, Staphylococcus aureus* and *Pseudomonas aeruginosa.* A summary of the assay range and concentration of each biomarker is shown in Table 1.

Table 1. List of sepsis biomarkers and bacteria selected to be detected by the AMBROSIA system.

Biomarker	Concentrations	
CRP	**Assay range**	**<0.2 to >20 mg/dL**
	Normal level healthy subjects	< 0.5 mg/dL
	Non-infectious SIRS	1 to 10 mg/dL
	Bacterial infection	4 to >20 mg/dL
	Sepsis/septic shock	8 to > 20 mg/dL
IL-6	**Assay range**	**5 to 1000 pg/mL**
	Healthy subjects	< 5 pg/mL
	Non-infectious SIRS	40-80 pg/mL
	Sepsis/septic shock	> 120 pg/mL
PCT	**Assay range**	**0.02 to 75 ng/mL**
	Healthy subjects	<0.1 ng/mL
	Bacterial infection	<0.1 to > 75 ng/mL
	Sepsis/septic shock	> 0.5 ng/mL
MR-pro-ADM	**Assay range**	**0.1 to 20 nM**

	Healthy subjects	< 0.5 nM
	Non-infectious SIRS	0.6- 1.1. nM
	Sepsis/septic shock	> 1.1 nM/L
Bacteria	**Specie**	**Concentration**
	Escherichia coli	10-10^4 cfu/mL
	Pseudomonas aeruginosa	10-10^4 cfu/mL
	Staphylococcus aureus	10-10^4 cfu/mL

C-reactive protein (CRP) is an acute phase protein produced by the hepatocytes after the stimulation by IL-6 and IL-8 as a consequence of an infection (bacterial or viral) or any other inflammation process (acute or chronic). CRP binds to bacteria promoting its aggregation and phagocytosis by leukocytes. CRP secretion starts within 4–6 h after stimulation peaking after 36-50 h. CRP concentrations in healthy subjects is <0.5 mg/dL and can reach levels higher than 50 mg/dL during inflammation. Despite CRP concentration can be increased by other non-infectious conditions, several studies have reported higher levels of this biomarker in septic patients as compared to critically ill patients with non-infectious SIRS independently of the clinical score.

In a study from Meynaar et al in which the usefulness of CRP for differentiating between sepsis and non-infectious SIRS was evaluated in critically ill patients in the first 24h of admission, they found that in the SIRS group the median concentration of CRP was 8 mg/dL (5.2-15.2) whereas in the sepsis group, it reaches the 17.9 mg/dL (8.8-29.7) (P<0.001) [12]. In a similar study conducted by Sierra et al, serum CRP concentration was measured in healthy subjects, acute myocardial infarctions (AMI), non-infectious SIRS patients, and sepsis patients [13]. They found that in healthy subjects the median values of CRP were 0.21 mg/dL (95% CI, 0.21-0.4), 2.2 mg/dL (95% CI, 2.1-4.9) in AMI, 1.7 mg/dL (95% CI, 2.4-5.5) in non-infectious SIRS patients and 18.9 mg/dL (95% CI, 17.1-21.8) in septic patients. They conclude that the best threshold value for CRP for predicting sepsis was 8 mg/dL (sensitivity 94.3%, specificity 87.3%).

Different cut-off values have been proposed for CRP. Most of the studies conclude that by itself, CRP shows a lower specificity for infection diagnosis and prognosis ability than other biomarkers, such as procalcitonin (PCT). Depending on the studies, the sensitivity of CRP varies from 62 to 100 % and its specificity from 4 to 100 % [14]. However, several studies have shown better results when CRP is used together with other biomarkers, with severity scores or with increased temperature. In that sense, Povoa et al reported in medico-surgical critically ill patients that serum CRP concentration of >8.7 mg/dL and temperature >38.2°C were associated to infection with a sensitivity and specificity of 93.4% and 86.1%, and 86.1% and 88.9 % respectively and that the combination of CRP >8.7 mg/DL and temperature >38.2°C increases the specificity for infection diagnosis to 100% [15].

It has been reported that in infected patients, CRP concentrations increases over time but remains unchanged in non-infected patients [15]. A daily CRP variation of at least 4.1 mg/dL was predictive of nosocomial infection with a sensitivity of 92% and specificity of 71%; when combined with a serum CRP above 8.7 mg/dL, the sensitivity and specificity increased to 92 and 82%, respectively [16]. Similarly, in patients with CRP concentrations >10 mg/dL on ICU admission were associated with a significantly higher incidence of respiratory (65% vs 28.8%, $p < 0.05$), renal (16.6% vs 3.6%, $p < 0.05$), and coagulation (6.4%

vs 0.9%, $p < 0.05$) failures and with higher mortality rates (36% vs 21%, $p < 0.05$) than patients with CRP levels < 1 mg/dL. In addition, in patients with CRP concentrations > 10 mg/dL a decrease in CRP after 48 h was linked to a mortality rate of 15%, while its increase was associated with a mortality rate of 61% ($p < 0.05$) [17]. In terms of prognosis, similar studies have confirmed that CRP does not allow early discrimination of survivors from non-survivors. A study from Tschaikowsky et al reported that the highest levels of CRP 2 and 3 days after the onset of postoperative sepsis (median values >10 mg/dL) do not distinguish between survivors and non-survivors, whereas after day 7, non-survivors show significantly marked re-increase levels of CRP than survivors. Authors suggest that this is most likely as part of an inflammatory response to a recurrent or unresolved infection in the non-surviving group [18]. A similar investigation confirmed in patients with severe sepsis that on day 7, CRP had a predictive value in terms of outcome with accuracy higher than IL-6, PCT, and acute physiology and chronic health evaluation (APACHE II) score [19].

Some authors have suggested that kinetics of CRP levels could help to evaluate the successful of antimicrobial therapy. The levels of this biomarker decrease more rapidly and to a greater degree in critically ill patients with sepsis admitted at medico-surgical departments of ICU with a favorable response to initial antibiotics [20]. In this study, the mean baseline of CRP concentration for the whole population was 16.7 mg/dL and an increase in CRP of at least 2.2 mg/dL in the first 48 h was associated with ineffective antibiotic therapy, with a sensitivity of 77% and a specificity of 67%.

Procalcitonin (PCT) is a prohormone of calcitonin synthesized at the thyroid. During a sepsis process, the main producers of PCT are macrophages and monocytes cell from different organs, and mainly from the liver. In healthy people, PCT levels are undetectable because it is processed as soon as is synthesized. The synthesis of PCT can be identified after 2-3h after onset of infection what makes PCT a useful biomarker for early sepsis diagnosis. The maximum peak of this biomarker is reached after 8 and 24h after infection onset and the concentration fluctuates in the range of 10-100 ng/ml. PCT is very stable and possesses a median half-life of ≈24h. It is important to note that PCT does not increase during a viral infection.

PCT levels in blood are undetectable at <0.1 ng/ml in healthy subjects. In adult ICU patients, many studies have evaluated the diagnostic value of serum PCT levels for sepsis, reporting sensitivity and specificity values ranging from 44 to 100% and 53 to 100%, respectively, with cutoff values ranging from 0.25 to 9.7 ng/mL. A median cutoff of 1.1 ng/ml (IQR 0.5–2.0) on ICU patients with sepsis, severe sepsis and septic shock across different studies has been reported in a meta-analysis with a mean sensitivity of 77 % (95 % CI, 72–81 %) and mean specificity of 79 % (95 % CI 74–87 %) [21].

Several studies have reported that higher PCT levels could differentiate Gram-negative sepsis from Gram-positive and fungal sepsis. Brodská et al found in septic patients with positive blood cultures a median PCT concentration of 8.90 ng/ml (IQR, 1.88-32.60) in Gram-negative, 0.73 (IQR, 0.22-3.40) in Gram-positive, and 0.58 (IQR, 0.35; 0.73) in fungi ($p \leq 0.00001$) infections [22]. Similarly, Charles et al. reported in critically ill patients admitted at ICU with clinical sepsis at the onset of blood stream infection, median PCT levels in the Gram-negative group of 39.00 ng/ml (range: 0.41-746.0), 5.42 ng/ml (range: 0.07–169.00) in the Gram-positive ($p=0.003$). In addition, when a PCT level of 16.0 ng/mL was used it was estimated at 83.0% positive predictive value and a 74.0% negative predictive value for gram-negative-related bacteremia (AUROCC = 0.79; 95% CI, 0.71–0.88) [23]. Reinhart et al conducted a meta-analysis in which PCT levels in patients with bacterial infection and different severities of systemic inflammation were compared [24]. They showed that in patients with sepsis, PCT levels ranged between 0.8 and 6.6, in those

with severe sepsis between 5.58 and 37, and septic shock patients had the highest PCT levels averaging between 4 and 45 ng/ml.

The level of PCT increases with the severity of the infection showing a better prognostic value than CRP. For this purpose, trends in concentrations over time have been demonstrated to be more valuable than single measurements. In a study of 289 patients with sepsis conducted in Greece in 2011, it was shown that mortality rates were 12.3% in patients whose PCT levels decreased by more 30% or was below 0.25ng/ml on day 3 compared to day 1 of sepsis diagnosis. In patients in whom PCT concentration had decrease <30% or was higher than 0.25ng/ml on day 3 compared to day 1, mortality rate was 29.9% (21). Similar results were found by Giamarellos-Bourboulis et al., reporting mortality rates of 26 % in ICU patients with PCT ≤0.85 ng/mL but 45 % in those with PCT >0.85 ng/mL (p = 0.002) within 24 h of onset of sepsis [25].

Trends in concentration of PCT has been evaluated to guide antimicrobial therapy what is extremely interesting for minimize adverse effects on patients, reduce the selection of antibiotic resistant microbes, and reduce costs. The PRORATA trial, a large randomized PCT trial performed in eight French ICU in France, compared PCT-guided antibiotic therapy to usual care in predominantly non-surgical patients with suspected bacterial sepsis. In this study, if PCT concentration is ≤0.25 ng/ml, antibiotics are strongly discouraged because the low probability of a bacterial infection, while if the PCT concentration was ≥0.5 ng/ml the use of antibiotics was encouraged and if it was ≥1 ng/ml antibiotics were strongly encouraged. It was demonstrated that PCT guidance significantly reduced antibiotic use (absolute difference 2.7 days, 95% CI 1.4 to 4.1, p<0·0001) but had no effect on mortality rate [26].

Interleukin-6 (IL-6) is produced by various types of cells including monocytes, fibroblasts, endothelial cells, keratinocytes, T-lymphocytes and tumour cells. Together with TNF-α and IL-1β, mediate the initial response of the innate immunity to injury or infection, enhancing the liver's production of the acute phase reactants, including CRP. These three cytokines are essentially the responsible for the features of SIRS. IL-6 can be measured in plasma very reliable however, like TNF-α and IL-1β, IL-6 is not specific for sepsis and levels are also increased in other inflammatory processes, such as arthritis and myocardial infarction. Nevertheless, lower levels of IL-6 have been observed in non-infectious SIRS as compared to sepsis. Rodríguez-Gaspar et al determined IL-6 levels in healthy subjects, patients with non-infectious SIRS, with sepsis, with severe sepsis, and with septic shock. The mean serum levels where 2.8 (+-0.3), 63 (+-15), 183 (+-66) and 409 (+-131) pg/ml respectively [27]. Also, in severely traumatized patients, IL-6 levels are higher in patients with infectious on day 1 after trauma than in patients without infection (551.6 ± 124.1 pg/ml and 282.1 ± 39.8 pg/ml respectively) [28].

IL-6 responds very fast to infection and is released into the bloodstream for 4–6h; with levels subsequently decreasing over the next 24–48 h. The utility of IL-6 compared with PCT and IL-8 to differentiate patients with sepsis from those with SIRS was assessed also in a study in critically ill patients [29]. PCT appeared to be the most helpful with a cut-off value of 1.1 ng/ml (AUC, 0.92; CI, 0.85 to 1.0), followed by IL-6 with a cut-off value of 200 pg/ml (AUC, 0.75; CI, 0.63 to 0.87). However, in other study, IL-6 with a cut-off >500 pg/ml had similar discriminating power as PCT to differentiate between sepsis and non-infectious SIRS in ICU patients [30]. These findings were confirmed in a cohort study comparing different biomarkers including IL-6 [31]. In that study the used cut-off value was 140 pg/ml (AUC, 0.76; CI, 0.7-0.82) and the sensitivity and specificity values were 71% and 72% respectively.

IL-6 has further been shown to be an independent predictor of poor outcome in unselected critically ill patients. In a study conducted in Greece, the median IL-6 level in survivors and non survivors were 146 pg/ml and 412 pg/ml, respectively (p<0.001) [32]. Similarly, Jekarl et al reported that after antibiotic

treatment in patients with sepsis and septic shock, IL-6 showed better kinetics in follow-up evaluations compared to PCT and CRP [33]. They evaluated these biomarkers after antimicrobial treatment at the time of the initial visit (0 h) and after 12, 24, 48, 72, and 96 h. These follow-up data showed that the total mean values of PCT and IL-6 were significantly different among survivors and non-survivors. The total mean values of PCT were as follows: survivor, 7.3 pg/mL; non-survivor, 22.3 ng/mL, respectively. The total mean values of IL-6 were as follows: survivor, 305.2 pg/mL; non-survivor, 1018.8 pg/mL.

Adrenomedullin (AM) is hypotensive peptide acting locally as a vasorelaxant and as a systemic vasodilator, produced by vascular smooth muscle cells and endothelial cells. Its widespread production in the tissues helps to maintain a blood supply in every organ. In addition, AM possesses immune modulating activity. It has also bactericidal activity, which is further enhanced by its regulation and modulation of complement activity. Prohormone fragments of AM (pro-ADM) are more stable than the complete peptide and their levels can be measured in biological fluids. The mid-regional fragment of proadrenomedullin (MR-pro-ADM), included between amino acids 45–92, is the most stable part of the ADM and it has been detected in plasma of patients with septic shock as a consequence of the ADM active peptide degradation. The measurement of ADM is technically challenging and reliable measurement is almost impossible because it is rapidly cleared from the circulation. A measurement of MR-proADM, which is much more stable, directly reflects levels of the rapidly degraded active peptide.

The diagnosis value of MR-proADM levels has been reported by several authors. Christ-Crain et al. performed a study in a cohort of 101 critical ill patients admitted to ICU compared with 160 age-matched healthy control individuals [34]. This work revealed that in patients with SIRS, the median MR-proADM levels was 1.1nm/L (range, 0.3–3.7); in those with sepsis 1.8 nm/L (range, 0.4–5.8), in those with severe sepsis 2.3 nmol/L (range, 1.0–17.6) and in patients with septic shock 4.5 nmol/L (0.9– 21). By the other hand in healthy control individuals the median of MR-proADM was 0.4 nmol/L (0.21–0.97). In addition, it was demonstrated that circulating MD-proADM levels on admission in patients with sepsis, severe sepsis, or septic shock was significantly higher in non-survivors (8.5 nmol/L [0.8–21.0]) than in survivors (1.7 nmol/L [0.4–17.6]) ($P < 0.001$). Therefore, MR-proADM levels correlate with increasing severity of illness and death.

Currently, the diagnostic methods used to detect infectious agents in sepsis cases rely mainly on culture, and/or polymerase chain reaction (PCR). While these methods are generally reliable, they have limitations such as time-consuming processes, the need for specialized laboratory equipment, and high pathogen loads, all of which contribute to delays in sepsis diagnosis. Considering the technical capabilities of the AMBROSIA PoC system, we propose the inclusion of a direct detection approach, without the need for prior amplification, targeting specific pathogens. Implementing this approach would overcome the delay in identifying the causative agent involved in sepsis compared to traditional blood culture methods. Moreover, it has the potential to enhance identification accuracy, as blood cultures often yield negative results in patients with sepsis.

Respiratory, intra-abdominal, urinary tract, and bloodstream infections, represented the major source of infection and sepsis, accounting for >75% of cases. Respiratory tract sources are by far the most frequent, with rates varying across sepsis categories, according to the time of infection, from 40–65%. Episodes including pneumonia range from 9–40%. Urinary tract infections varies between 10–15%. Primary bloodstream infection rates range between 2% and almost 20%, depending on whether catheter-related infections are included in the definitions.

Among the most prevalent bacteria associated with sepsis, the AMBROSIA project will investigate the feasibility of identifying *Staphylococcus aureus*, *Escherichia coli* and *Pseudomonas aeruginosa*. All of them

are common pathogens associated with sepsis. They can enter the bloodstream through various means, such as wounds, surgical sites, the urinary tract, abdominal cavity, respiratory tract, or intravenous catheters among others, and disseminate throughout the body. Once in the bloodstream, the bacteria can multiply rapidly, triggering a cascade of immune responses that can lead to widespread inflammation and organ dysfunction. In addition, during the last decades, these bacteria have evolved developing resistance mechanisms to antibiotics, thus reducing the choice of antimicrobial drugs to be adopted for an effective therapeutic treatment. Table 1 provides the compilation of the bacteria currently being considered for the AMBROSIA project.

3.3. Other system requirements related to the clinical context of Sepsis diagnosis

Sepsis is one of the most expensive hospital-treated conditions due to delayed effective treatment of patients, waiting for as many as five days to accurately identify pathogens. Depending on the phases of the Sepsis, different methods are used: biochemical and clinical assessment, immune assessment, microbiological assessment, hematological assessment, or molecular biology techniques. These techniques are expensive; some of them lack standardization and need skilled personnel to perform them. The multiplexed simultaneous traceability of the proposed biomarkers, ideally also identifying the infectious pathogen, close to the patient will aid in an improved, faster, and specific diagnosis of sepsis. According to this, the device should provide a direct response of the concentration of the selected biomarkers and the identification of the bacteria (presence or not, and, if present, its concentration) in a short period of time (less than 20-30 min). Sensor chips should be functionalized with specific receptors for each of the target biomarkers and bacteria selected and readily available to perform the analysis of different samples.

The type and volume of samples should also be defined. A maximum volume of <500 µL should be considered although in the case of pediatric patients, sometimes the whole blood volumes that can be collected are significantly lower than 500 µL. Specifically, medical doctors work with typical blood volumes around 20 µL for infants and 100 µL for children. This should be had in mind during the design of the system and the microfluidics, to reduce as much as possible, the volume of blood needed for accurate Sepsis detection.

Another requirement defines the sample type as “Serum, Li- or Na- heparinized plasma, EDTA plasma”. Although a real point-of-care system might be expected to accept directly whole blood samples, there are several arguments in favour of using serum or plasma samples, at least in the initial stage of the project:

- Based on discussions with medical professionals, it was found that many hospitals and even doctor premises have a centrifuge available to extract plasma from whole blood. Furthermore, even if not initially available, centrifuges are cheap to buy and easy to use.
- Blood cannot be stored for a long time, only plasma. Thus, for testing it would be necessary to work with plasma or substitutes anyhow.
- Blood separation on chip is possible in principle; thus, could be considered during the design of the microfluidics, although it would significantly increase the technical complexity and thus the cost of the microfluidic cartridge.

To validate this approach, a clear protocol describing the sample handling procedure from the patient to the microfluidic chip must be defined and confirmed by medical doctors, covering in particular:

1. The collection of patient blood in a standard container (e.g. vacutainer)
2. The plasma extraction in a centrifuge by untrained personnel

3. The connection to the microfluidic chip via a standard interface (e.g. Luer-lok)

Most of the sepsis cases are detected at the Hospital Emergency Departments and at the ICUs. The Point-of-Care platform should be an easy-to-use, fully integrated, automated (i.e. allowing the easy introduction of the sample in disposable cartridges, and an automatic visualization of the response) device as medical and nurse staff from these departments would be the main users. The POC device could be located either in these departments or at the central Laboratory in the hospital, as any other patient admitted to any other hospital department can develop an inflammatory response as a consequence of an infectious process. Having a device in every department is not the most feasible option. This option would benefit from the usual workflow of urgent samples in the hospital setting having the results in a timely manner.

According to these considerations, Table 2 summarizes the general features of the commercial Point-of-care device. These are requirements for an ideal final version to consider during the prototype development, although they are not all strictly needed for the success of this project.

Table 2. Preliminary defined requirements for the PoC platform.

General System specifications	
Integration	Fully integrated and automated point-of-care reader
Usability	Automated measurements; user-friendliness for non-specialized staff (*i.e.* sanitary personnel). Ready-to-use instrument.
Multiparametric analysis	Multiplexed detection of 4 biomarkers + identification of pathogen (1 out of 3) bacteria within the same sample. Simultaneous analysis.
Chip	Size: to be defined (17mm x 22mm for the 1st run) Minimum number of sensors: 7 Prepared to use (biofunctionalized with receptors).
Microfluidic cartridges	First approach: Reusable cartridge for testing Final approach: Disposable cartridge final prototype Both with the biofunctionalized chip incorporated Dimensions: 22x15.5 mm of sensing chip Material: • First approach: PDMS, PMMA • Final approach: PMMA, COC Measurement chamber: 8 channels with a width of 250 microns and 14 mm of length Sample loading: Direct connection of 1/16" tubing on the PDMS by tightening for both sample inlets and waste collection at the outlets
Size/weight	30cm×15cm×20cm (L×W×H), Weight no more than 2kg – Subject to change depending on the final set-up
Instrument power	10 – 30 W, Subject to change depending on the final set-up
Display	To be defined: External PC, Incorporated

Software requirements	To be defined
Other system specifications	To be defined

4. Technical specifications, conceptual designs and integration process flow related to the plasmo-photonic sensor chip

4.1. Technical specifications and conceptual designs

AUTH was responsible for the design and performance optimization of the AMBROSIA plasmo-photonic sensor circuits. Following the project's original Description of Action (DoA), two sensor configurations have been investigated: (i) a SiN-based, power-balanced plasmo-photonic Mach-Zehnder Interferometer (MZI) with aluminium (Al) plasmonic stripe waveguides on both arms, and (ii) a single-arm bimodal plasmo-photonic interferometer. Both configurations were first evaluated with bare plasmonic stripes without Bragg-gratings. The basic principle of operation, a brief description of the design process and the obtained specifications are given below. The detailed design analysis will be included in D3.1.

- **Balanced MZI sensor**

Regarding the first configuration, both branches of the MZI will host photonic strip waveguides (WG) based on LGT's SiN platform and plasmonic stripe WGs based on Aluminium (Al). Thermo-optic phase shifters will be introduced at every MZI branch in order to enable real-time tuning of the spectral dip at the wavelength of interest (1550 nm).

To efficiently transfer light from the photonic WG to the plasmonic WG and back, the photonic WG has been linearly tapered to 7.5 μm width with the aid of a photonic linear taper in order to achieve spatial mode matching between the supported photonic and plasmonic modes. Additionally, a vertical offset (VO) between the two waveguides was introduced in order to center-align the two modes of interest, maximizing power coupling. Through 3D FDTD simulations, the optimum value of the VO was found equal to 350 nm resulting in 40% coupling efficiency. This means that the introduced losses due to the plasmo-photonic interfaces are 4 dB/interface and 8 dB in total. The propagation losses of the plasmonic mode were calculated equal to 0.06 dB/ μm resulting in 4.2 dB extra losses for a 70 um plasmonic stripe and total Insertion Losses (IL) equal to 12.2 dB for the whole sensor.

Afterwards, the complete MZI was also evaluated via circuit-level simulations by using the INTERCONNECT photonic integrated circuit simulator of Lumerical. Several sensor variants with different free spectral ranges (FSR) have been investigated. In all cases, plasmonic stripes of 70 μm length have been considered whereas the FSR was tuned by introducing a length difference (ΔL) through the photonic waveguide of the reference branch. Figure 1(a-c) presents the spectral response of three sensor variants with FSRs equal to 44 nm, 147 nm and 300 nm along with the spectral shift when aqueous solutions with varying refractive index (RI) are considered on top of the plasmonic waveguide in the sensing arm. Table 3 summarizes the specifications of all the investigated sensor variants. As can be seen, the simulation results showed that the bulk RI sensitivity increases with increasing FSR and decreasing ΔL, reaching the value of 28000 nm/RIU with an expected limit of detection of 3.5×10^{-7}, considering a system resolution of 10 pm. In one sensor variant, the plasmonic length was doubled resulting in double RI sensitivity, as expected.

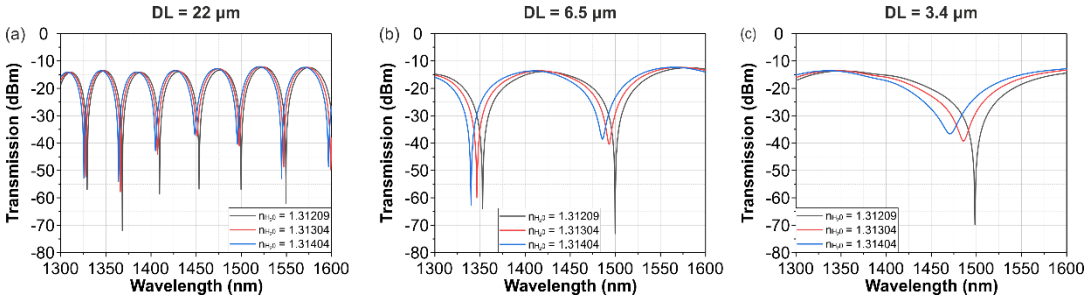

Figure 1. Simulated transfer function and sensitivity measurements of the MZI sensor for different ΔL and FSRs: (a) ΔL = 22 μm, FSR= 44 nm, (b) ΔL = 6.5 μm, FSR= 147 nm and (c) ΔL = 3.4 μm, FSR= 300 nm.

Table 3. Key specifications of all the investigated MZI sensor variants.

Parameter	Sensor 1	Sensor 2	Sensor 3	Sensor 4	Sensor 5	Sensor 6	Sensor 7	Sensor 8
Plasmonic Length (μm)	70	70	70	70	70	140	70	70
ΔL (μm)	22	16	10	6.5	5	5	3.4	2
FSR (nm)	44	70	100	147	186	186	300	>300
Sensitivity (nm/RIU)	2067	3037	4682	7274	9323	18646	14201	28000
Limit of detection	4.8×10^{-6}	3.3×10^{-6}	2.1×10^{-6}	1.4×10^{-6}	1.1×10^{-6}	5.4×10^{-7}	7×10^{-7}	3.6×10^{-7}

Bimodal sensor

The alternative plasmo-photonic bimodal interferometric sensor consists of two access SiN photonic waveguides which are separated by an aluminium-based stripe residing on top of a thinner dielectric layer, hereafter referred to as Bottom Layer. This more compact configuration will exploit not only the top but also the bottom metal surface to form two distinct optical paths on the same waveguide. These two metal-insulator interfaces are both able to support SPP modes which, upon simultaneous excitation through the input photonic waveguide, will propagate along the two metal surfaces and interfere at the output photonic waveguide realizing a single-arm interferometer. The top mode will act as the sensing arm, whereas the bottom mode will act as the reference arm.

Three performance metrics were considered during the design process: (i) maximum sensitivity, (ii) maximum ER, and (iii) FSR smaller than a typical tunable laser range at C-band. The ER depends on the coupling coefficients from the photonic mode to the two plasmonic modes and vice versa, the propagation losses of the plasmonic modes and the length of the plasmonic stripe. Optimal interference and, thus, maximum ER can be achieved by tuning the coupling coefficients and the propagation losses by means of the appropriate thickness of the bottom layer. Thus, the ER was calculated as a function of the bottom layer thickness and for various aluminium stripe lengths ranging between 10 and 200 μm length. The optimum bottom layer thickness was selected so that the ER is maximum, while the preferred plasmonic lengths were selected so that the FSR is rather small. For the optimum configuration, the required bottom layer thickness was found equal to 320 nm leading to 17% power coupling from the photonic to the top plasmonic mode and 14.75% power coupling from the photonic to the bottom plasmonic mode corresponding to ~5 dB losses/per interface. The propagation losses were calculated equal to 0.07 dB/ μm for the top plasmonic mode and 0.064 dB/ μm for the bottom plasmonic mode. The total Insertion Losses

(IL) vary between 16.6 dB and 23.3 dB for sensors with plasmonic stripe lengths between 100 µm and 200 µm.

The optimum bimodal sensor was further evaluated through circuit-level simulations. The obtained transfer functions for three different aluminium stripe lengths (100 µm, 120 µm, 140 µm) along with the spectral shift when aqueous solutions with varying refractive index (RI) are considered on top of the aluminium surface are illustrated in Figure 2(a)-(c). The simulated bulk RI sensitivity was equal to 13123 nm/RIU irrespective of the sensing length corresponding to an expected limit of detection of 7.6×10^{-7}.

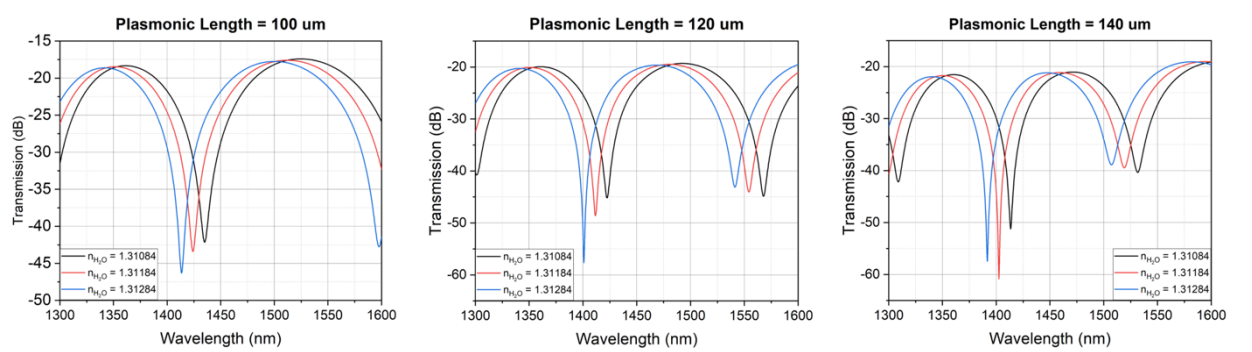

Figure 2. Simulated transfer function of the optimum bimodal configuration for different plasmonic lengths and using different liquid samples above the sensing area: (a) L = 100 µm, (b) L = 120 µm, FSR= 140 nm and (c) L = 140. The sensitivity in all cases is equal to 13123 nm/RIU.

Summary of the technical specification for both sensor configurations

Table 4 summarizes the technical specifications of both AMBROSIA sensor configurations.

Table 4. Technical specifications of AMBROSIA sensors.

Parameter	Balanced MZI	Bimodal
Photonic WG dimensions (*W* × *t*)	1 µm × 800 nm	1 µm × 800 nm
Plasmonic WG dimensions (*W* × *t*)	7 µm × 80 nm	7 µm × 80 nm
Vertical Offset (nm)	350 nm	-
Interface losses (dB)	4 dB/interface	5/interface
Plasmonic propagation losses (dB/µm)	0.06 dB/µm	0.07 dB/µm (top) 0.064 dB/µm (bottom)
ΔL (µm)	2 – 22	-
Bottom layer thickness (nm)	-	320 nm
Plasmonic WG length (µm)	70 / 140	100 – 200
FSR (nm)	>300 – 47	199 – 100
ER (dB)	50 – 60	29 – 64
IL (dB)	12.2 – 16.4	16.6 – 23.3
Sensitivity (nm/RIU)	2067 – 28000	13123
Limit of detection (RIU)	4.8×10^{-6} – 3.6×10^{-7}	7.6×10^{-7}

Asymmetric MZI sensor with Bragg-grating

UOI investigated an asymmetric MZI sensor with Bragg-grating Aluminum plasmonic stripes on both arms. The asymmetry is obtained by adding an extra length of the photonic waveguide in one of the two arms. The extra length is calculated so as to force light interference at a specific wavelength, keeping in mind that the larger the asymmetry the smaller the FSR. In this work, we scan all the wavelengths to find the optimal operation point.

To estimate the sensitivity, a change of the environment refractive index is applied along the sensing area (Bragg cavity) on the sensing arm. The sensitivity is calculated via the reflection and transmission mode in two ways according to a) the shifted resonance (nm/RIU) and b) the modulation depth of transmission and reflection (dB/RIU) after the index change. The light enters into the multi-layer structure from the left port. An amount of the light is reflected, and the rest is transmitted after traveling back and forward in the region of cavity causing a phase accumulation based on the slow light effect which enhances the sensitivity of the plasmo-photonic sensor.

Our study was focused on two slow-light regions, in the cavity mode and at the edge of band gap, where the slow light effect works well. To study the full parameter space of the Bragg cavity, a semi-analytical model based on the transfer matrix method (TMM) was developed and validated via the 2D FDTD method. The 1D-model uses as input the effective refractive indices n_1 , n_2 with the corresponding thicknesses d_1, d_2 (Figure 3) for each plasmonic section (Al with water and dielectric). The thicknesses are calculated with respect to the Bragg condition for maximum reflection (quarter - wave - stack):

$$d_{1,2} = {\lambda_{Bragg}}/{4 * n_{1,2}}$$

were λ_{Bragg} is the central desired wavelength for the band gap of the Bragg cavity, in our study $\lambda_{Bragg} = 1550nm$. The length of the cavity (d_{cav}) is equal to $2 * d_1$.

The adjustable parameters of the system were the number of Bragg periods (N_{Bragg}), the number of cavities (N_{cav}), and the length ($L_{cav}=N*d_{cav}= N*2*d_1$) of the cavities (Figure 3). Also, considering the phase difference ($\Delta\varphi$) between the two arms the FSR was determined.

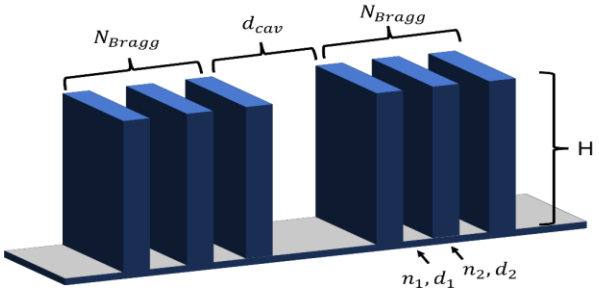

Figure 3. Schematic of the Bragg cavity with depiction of its adjustable parameters.

In the following study, Si_3N_4 and Parylene were assumed to formulate the Bragg grating. Through the optimization process, it was concluded that for both materials the sensitivities increase with respect to increasing N_{Bragg}, N_{cav}, and L_{cav} quantities. On the other hand, the sensitivity becomes lower with increasing phase difference. Also, the sensitivity is enhanced more strongly in the region of the cavity than in the region of the band gap edges. Finally, it was found that the scattering, which is caused by the edges of the teeth, strongly depends on the height of the teeth. Consequently, to mitigate the scattering, large height

for Bragg teeth is required, keeping in mind the fabrication restrictions. To achieve this, it is necessary to apply higher order of Bragg such as 3rd and 5th.

After the optimization process and the analysis, two designs are proposed for testing, consisting of different number of cavities (two and four). In both cases, 3 variations for the length of the cavities are suggested (for N=2, 4, 8 with respect to $L_{cav}=N*d_{cav}$). For each individual design the Si_3N_4 and Parylene will be used for the Bragg grating.

Finally, for the 5th order Bragg cavities with Si_3N_4 we performed 2D FDTD simulations and we calculated the sensitivities for systems with semi-infinite and finite teeth. We conclude that even though the sensitivity decreases when scattering is caused by the edges of the teeth, it remains at least 2 times higher than the sensitivity we get from a plasmonic sensor without the Bragg configuration (Table 5).

Table 5. Results for the sensitivity for 5th order Bragg calculated from transmission.

H_{tooth}	S_{cav_T} (nm/RIU)	$S_{w/o\ Bragg}$ (nm/RIU)
Semi-infinite	$2.1x10^5$	$0.65x10^5$
Finite	$1.6x10^5$	$0.65x10^5$

4.2. Integration process flow

Integration of the aluminium strip into the etched cavity

Microfabrication of the aluminium plasmonic sensor starts with defining plasmonic cavities on Ligentec's AN800 (all nitride 800 nm Si_3N_4) platform. The stack consists of thick thermal oxide (commonly referred to as bottom oxide - BOX) grown on Silicon wafers. An 800 nm thick Si_3N_4 film deposited by Low Pressure Chemical Vapor Deposition (LPCVD). The stack is capped by a top oxide cladding of 2.2 um (also referred to as top oxide - TOX). Aluminium-based heaters are also integrated in the stack to allow for thermal tuning. The heaters are encapsulated by oxide and vias defined to allow for electrical probing.

First, a photoresist film is patterned on top of the cladding defining the cavity. Next, the oxide layer is etched down by an RIE process. In the MZi configuration, the etched depth is targeted 350 nm below the Si_3N_4 bottom level (Figure 4(a)). While in the bimodal configuration, the target etched depth is 400 nm above the Si_3N_4 bottom level (Figure 4(b)).

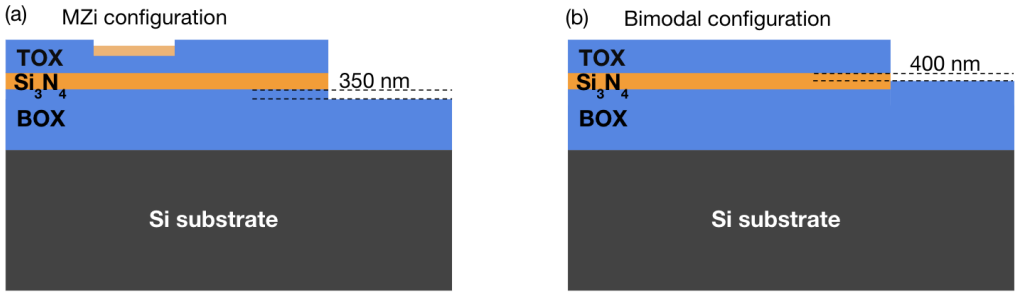

Figure 4. Cross-section diagrams of the (a) MZi and (b) bimodal configurations.

Metallisation of the plasmonic cavity is done by a lift-off process to prevent sidewall coverage of the cavity. Figure 5 depicts the process flow for the MZi configuration (the bimodal is omitted for sake of

simplicity, as it follows the same steps). Once the plasmonic cavity is defined (Figure 5(a)), a lithography step defines openings over the cavity (Figure 5(b)). Then, an aluminium thin film (80 nm) is evaporated onto the wafer (Figure 5(c)). Finally, the photoresist film is stripped by lift-off, removing the aluminium everywhere except from the plasmonic cavities (Figure 5(d)).

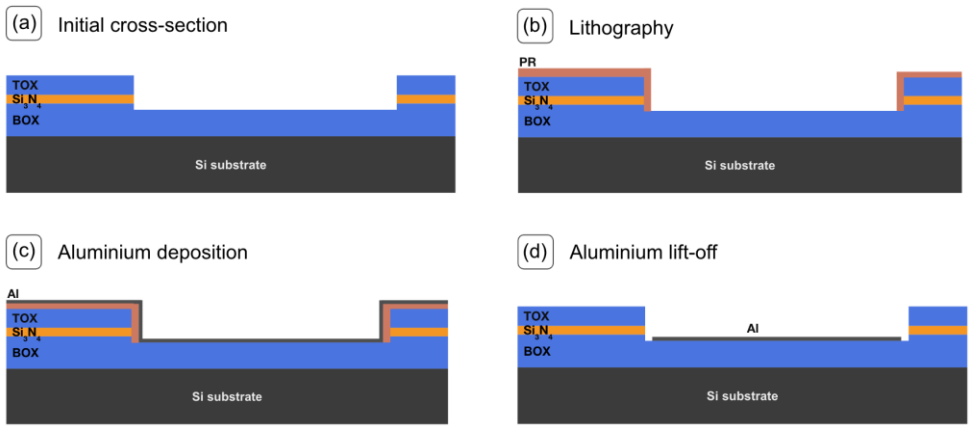

Figure 5. Schematic process flow of the plasmonic cavity metallisation. Refer to the main text for further details.

Tests were performed on samples, provided by Ligentec, in order to evaluate the capabilities of UB to integrate the µm × 80 nm aluminum stripes into the cavities etched in SiN layer by using the etched alignment marks for automatic alignment procedure implemented in UB e-beam lithography system.

Figure 6 provides the process flow for the integration of the metal strips into the cavity. The process goes as following:

1. Electron-beam lithography steps (resist deposition + exposure) required for fabrication of aluminum strips on 22 x 22 mm Si/SiO_2 diced chips, provided by Ligentec, which already include etched cavities and etched alignment marks. Subsequent development of the resist.
2. Deposition of an 80 nm layer of Aluminium on top of the exposed and developed resist layer.
3. Lift-off process of aluminium, which results into piling off of the aluminium layer covering the unexposed part of the sample, leaving only the aluminium on the exposed parts.

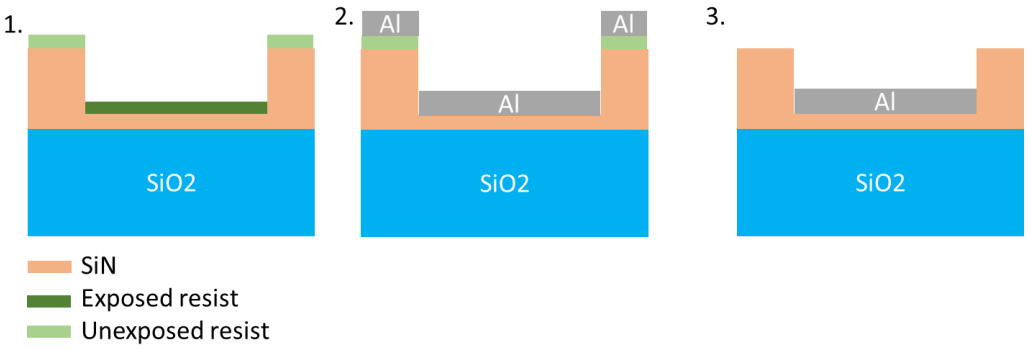

Figure 6. Process flow for integration of the aluminum strips into SiN cavities.

Integration of the Bragg grating

The Bragg grating integration process will strongly depend on the choice of material of the grating itself. The choice will be based on the optimal configuration derived from the analytical and numerical simulations performed by the collaborators within the project.

In the optical characterization experiments, that are currently in progress in UB, the process flow is the following (Figure 7):

1. Electron-beam lithography steps (resist deposition + exposure) required for fabrication of aluminum strips on 22 x 22 mm Si/SiO_2 diced chips.
2. Deposition of a layer of high refractive index silicon nitride (SiN) at a required thickness (to be defined) and subsequent deposition of a resist mask corresponding to the Bragg grating design.
3. Formation of the gratings by the use of reactive ion etching (RIE) process by using the pre-designed resist mask. The design of the mask will dictate the design of the grating with a desired filling factor and period.

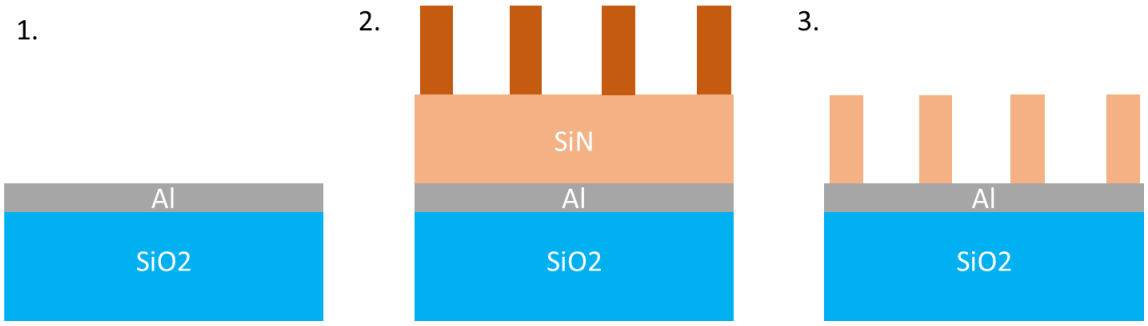

Figure 7. Process flow for the integration of the Bragg gratings onto aluminum strips.

This procedure is planned to be executed on both UB and Ligentec samples to test the reflection, transmission, and losses (RTL) properties of the Bragg gratings with the use of a fiber-to-fiber optical setup of UB.

5. Technical specifications, conceptual designs and integration process flow related to the neuromorphic chip

5.1. Design of SiN passives structures

In AMBROSIA we utilize a silicon nitride (Si_xN_y) platform to obtain the optimum between component density and index contrast, while ensuring low-loss and high-performance passive functionalities. SOTON developed two families of passive components, targeting TE and TM polarization, respectively. Their designs were optimised mainly by using numerical simulation methods such as finite different eigenmode (FDE) and finite-difference time-domain (FDTD). The calculated performance of the optimised designs for every component are displayed in Table 6.

Table 6. Simulated photonic devices in SIN.

Si_xN_y passive circuits			
Components	**Parameters**	**Sim. Values** (TE-polarization)	**Sim. Values** (TM-polarization)
GCs	Insertion Loss	4 dB/grating	6 dB/grating
	Angle	8.0°	28.3°
Single mode WGs	Width	1.0 µm	1.0 µm
WG Bends	Optimal radius	60 µm	60 µm
	Insertion Loss	0.053 dB/bend	0.072 dB/bend
MMIs (1x2)	Insertion Loss	0.03 dB	0.02 dB
	Splitting Ratio	1.0	1.0
MMIs (2x2)	Insertion Loss	0.052 dB	0.024 dB
	Splitting Ratio	0.9898	0.9979
WG Crossing	Insertion Loss	0.007 dB	0.01 dB
	Crosstalk	-33.5 dB	-35.5 dB

5.2. Fabrication and Characterization of passive SiN structures

This task dealt with the fabrication and characterization of a Si_xN_y passive structure portfolio, that aims to be employed across test structures and demonstrators, facilitating the required waveguiding, I/O coupling and splitting. SOTON fabricated each structure using the optimum parameters extracted by the simulations. The developed components, along with the experimentally derived specifications, are summarized in Table 7 for both TE and TM polarization.

Table 7. Summarized experimental specifications for passive SiN technology.

Passive SiN structures (layer stack: 3µm-SiO_2/400nm-Si_xN_y/3.2µm-SiO_2/Si-substrate)							
Components	Parameters	**TE**-polarization			**TM**-polarization		
		Sim. (@1550nm)	**Experiment** (@1550nm) RUN 1	RUN 2	Sim. (@1550nm)	**Experiment** (@1550nm) RUN 1	RUN 2
Grating coupler (coupling θ = 8.0°)	Centre wavelength (nm)	1560	1555	1555	1553	1561	1552
	Max. Coupling efficiency (dB/grating)	3.9	6.1	5.8	7.0	9.1	10.7
	1dB-bandwidth (nm)	54	58	74	52	56	68
Waveguide (1 µm-wide)	Propagation loss (dB/cm) [@1530-1595nm]	-	**2.96 [1.14 - 5.84]**	**0.96 [0.14 – 2.08]**	-	**1.75 [0.96 – 3.32]**	**1.12 [0.31 – 2.16]**
	Group index	-	2.018	1.987	-	1.926	1.990
WG Bend (radius 60µm)	Insertion Loss (dB/bend)	-	0.023	0.008	-	0.030	0.027
MMI (1x2)	Insertion Loss (dB)	0.030	0.085	0.091	0.020	0.065	-
	Splitting ratio	1.000	0.981	0.867	1.000	0.912	-
MMI (2x2)	Insertion Loss (dB)	0.052	0.620	0.253	0.024	0.140	-
	Splitting ratio	0.989	0.977	0.897	0.998	0.872	-
WG Crossing	Insertion Loss (dB)	0.007	0.13	0.18	0.01	0.18	0.20
	Crosstalk (dB)	-	-60	-45	-	-51	-40

Finally, Figure 8 depicts the designed GDS layout including all the test structures and its fabrication variants. The layout schemes of test structures are identical for both polarization designs, and they are intended to be fabricated on a single chip as shown in the figure below.

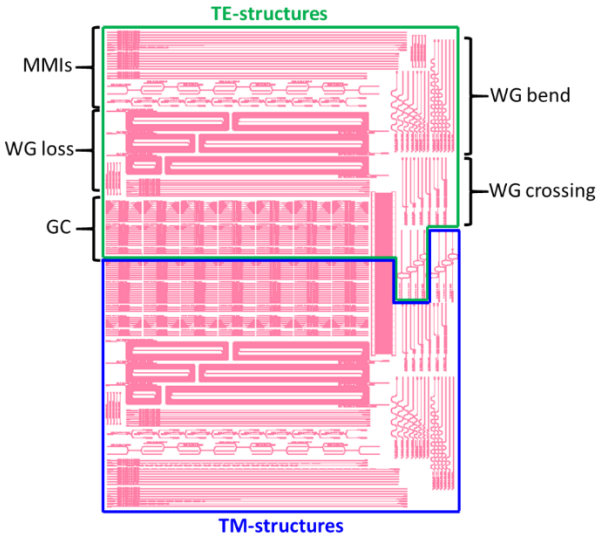

Figure 8. GDS layout of the mask designed and fabricated by SOTON, for testing SiN passive structures.

5.3. Process flow and simulation of electro optic phase change material phase shifters

Following the design of the passive Si_xN_y components, a process flow of the proposed PCM phase shifter architecture was developed where phase change materials and photonic structure will be co-integrated to form electro optic memories. Table 8 shows the simulated effective index change of the TE mode supported by the PCM-based phase shifters, and the insertion loss of this phase shifter when achieving 2π phase difference. Thicker PCM on top of waveguide can provide greater modulation effect, but also induce higher insertion loss. Therefore, in this project we will go for 20 nm thick PCM to achieve lower loss.

Table 8: Simulated result for PCM phase shifters in C-band

Thickness of PCM (nm)	Wavelength &Material	Length for 2π phase shift (μm)	Insertion Loss (dB/μm)	Insertion Loss for 2π phase shift (dB)	Effective index (Crystalline)	Effective index (Amorphous)
20	C_band SbSe	35	0.07	2.45	1.77	1.73
	C_band SbS	39.6	0.016	0.63	1.74	1.71

5.4. Design and specifications of the photonic neuromorphic circuit

For the implementation of the photonic neuromorphic circuit, two Crossbar (Xbar) architectures have been investigated with regard to their dimensions (inputs x outputs): (i) 4 x 8, and (ii) 8 x 4. In both cases, one laser will feed all Xbar inputs. Thermo-optic (TO) modulators will be used at the inputs. In the 8 x 4 layout, the 8 TO modulators will be driven by the sensor outputs (concentration of the 7 targets). The weighting elements will be implemented by PCM-based MZIs. Length matching of intra column paths and

time synchronized paths are needed. Power balance at each column output is accomplished by cascaded 3 dB MMIs.

6. Technical specifications, conceptual designs and integration process flow of electronics - PCB

6.1. Introduction

This part of the report presents the technical specifications for the design and manufacture of printed circuit boards (PCBs) intended for casual use, specifically for the implementation of DC current applications. The requirement includes the separate PCBs for the heater drive, the PCM drive and a separate PCB for the control of the lasers, detectors, control structures and other remaining active and passive components necessary for the proper operation of the overall device.

Standard edge connectors and SMA connectors are used for the necessary input and output connections between the boards and between the boards and external devices.

6.2. PCB Design Considerations

PCB design will follow industry standard practices with emphasis on electrical performance, thermal management and mechanical stability. PCBs will be designed as multilayer boards to accommodate complex circuits and optimise signal integrity and noise immunity. The following materials and specifications will be considered to achieve these objectives:

PCB Materials:

- FR-4 (Flame Retardant 4): This widely used material provides good electrical insulation and mechanical strength.
- High-Tg FR-4: A variant of FR-4 with a higher glass transition temperature, suitable for applications with higher operating temperatures.
- Polyimide: Often used in flexible circuit boards, polyimide offers excellent thermal stability and flexibility.
- Thermoset-based hydrocarbon ceramic materials - characterised by excellent electrical performance, thermal stability and dimensional stability. One such material is Rogers 4350/4003.

The final choice of PCB material is made when the thermal model of the demonstrator is built. This is done when all the functional diagrams of all the circuits are completed and fixed.

Based on these diagrams and thermal simulations of this model, we will know how much heat needs to be dissipated, which will give us clear indications of which PCB material will be the most suitable.

Path Sizes and Contacting Pads:

- Typical PCB trace widths and spacings depend on the complexity and requirements of the final versions of the circuits. In general, standard trace widths range from 5 to 10 mils (0.127 to 0.254 mm).
- Contact pads, also known as landing pads or solder pads, are typically around 35 to 45 mils (0.889 to 1.143 mm) in diameter. However, the specific pad size can vary depending on the components used and the manufacturing processes employed.

Pitch:

- Pitch refers to the distance from the centre of one pad to the centre of the adjacent pad. It varies depending on circuit complexity, component density and manufacturing capabilities.
- For surface mount technology (SMT) components, common pitches are 0.5 mm, 0.8 mm, 1 mm or 1.27 mm. However, finer pitches such as 0.4 mm or 0.3 mm are becoming more popular for advanced circuits and are being investigated where miniaturisation is required.

Metal Finish Layers Ready for Wirebonding Process:

- OSP (Organic Solderability Preservative): A thin protective layer that allows direct wire bonding to exposed copper pads without the need for additional surface treatment.
- ENIG (Electroless Nickel Immersion Gold): Provides flat and reliable contact surfaces with excellent corrosion resistance. ENIG improves wirebonding compatibility.
- HASL (Hot Air Solder Leveling): Provides a cost-effective option suitable for wirebonding after proper preparation. However, it may not offer the same precision and flatness as OSP or ENIG.

At this stage of the project, ENIG would be the most likely option for finishing metal layers for wirebonding purposes.

By selecting appropriate materials, optimising trace sizes and pad designs, and ensuring suitable metal finish layers, the PCB design will be able to meet the desired electrical, thermal and mechanical performance requirements while taking into account wirebonding compatibility.

6.3. Heater Driving PCB

The PCB dedicated to heater control will allow to support the efficient operation of the heaters on the sensor photonic chip in a fully controllable way. Due to the need for precise positioning of the contact pins, it will be mounted on a manually controlled X-Y-Z stage to ensure easy and precise contacting of all the heaters at once (Figure 9). Considering the current status of the sensor chip design, the PCB should drive a 28-channel pad array on the sensor chip edge with a pad size of 150 µm x 150 µm and a pitch of 300 µm.

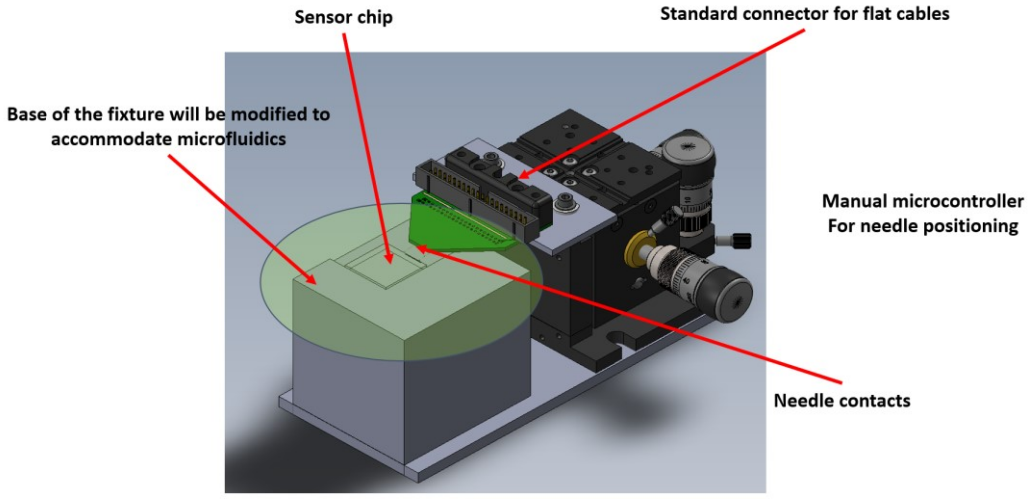

Figure 9. Design of assembly of the PCB with the sensor photonic chip.

6.4. PCM Driving PCB

The PCB for the PCM drive will also incorporate thermal management solutions to ensure optimum temperature control and prevent overheating. This will include the inclusion of heat sinks and thermal vias, supported by thermal simulation results.

The PCB will be designed using High Density Interconnect (HDI) technology, which allows for a compact layout and efficient use of space. This will enable a smaller form factor, making it suitable for integration into various devices or systems.

In addition, the PCB will incorporate advanced electromagnetic compatibility (EMC) shielding techniques to minimise electromagnetic interference (EMI) and ensure the reliability of the PCM drive system. This includes the use of grounding techniques, shielding layers and proper layout considerations to achieve optimum EMC performance.

Where necessary, the PCB design will include additional contact points to allow electrical diagnostics if required. This feature will be evaluated in more detail during the next phase of the project.

6.5. Laser and Detecting Structures PCB

In the field of lasers and detection structures, high frequency applications are often encountered, requiring a specialised printed circuit board (PCB) design. The PCB dedicated to this area is designed with meticulous attention to detail to ensure optimum performance. A key aspect of the design is impedance matching techniques. By carefully matching impedance, the PCB will maximise the efficiency of signal transfer. This reduces energy loss during transmission and minimises signal reflections, resulting in improved overall system performance.

To further enhance the functionality of the PCB, an optimised grounding scheme is incorporated into the layout. Grounding plays a vital role in minimising noise and interference, particularly in high frequency applications. By implementing an optimised grounding scheme, the PCB can effectively reduce electromagnetic interference and crosstalk. This ensures the accuracy and reliability of the signals transmitted and received by the lasers and detection structures.

In addition to impedance matching and grounding techniques, shielding is also a key consideration during the design process. Electromagnetic interference (EMI) is a common problem that can adversely affect the performance of high frequency circuits. Therefore, the PCB for lasers and detection structures will include shielding measures to protect the sensitive components from external EMI sources. This shielding can be achieved by incorporating conductive materials into the PCB design, such as copper plating or metal shielding, which provide a barrier to unwanted interference.

Careful attention is also paid to the layout of components on the PCB. The correct placement and routing of traces can contribute to the overall performance and efficiency of the system. By considering factors such as signal integrity and minimising the length of high frequency traces, the design will minimise signal degradation and maintain the integrity of the transmitted and received signals. This will ensure precise and accurate measurements in the detection of structures and optimum operation of the lasers.

In summary, the PCB dedicated to lasers and detection structures in high frequency applications will employ various techniques and considerations to ensure optimum performance. Impedance matching, optimised grounding schemes, EMI shielding and careful component placement are used in the design to maximise signal transfer efficiency, minimise interference and maintain signal integrity. By paying close attention to these aspects, the PCB will contribute significantly to the overall functionality and accuracy of laser systems and detection structures.

6.6. Input and Output Connectors

The use of standard connectors that are readily available on the market provides a seamless connection to external devices. The use of standard edge connectors and SMA connectors ensures convenient and standardised connectivity for the PCBs. Standard edge connectors are ideal for connecting power, control signals and low frequency heat sink connections. These connectors are widely available and are designed to fit into designated slots on the PCB, providing a simple and secure connection.

SMA connectors, on the other hand, are specifically designed for high frequency signal transmission and reception. By incorporating SMA connectors into the design, PCBs are able to communicate efficiently with lasers, sensing and control structures. SMA connectors offer excellent performance in terms of minimising signal loss and maintaining signal integrity, making them an ideal choice for high frequency applications.

By using standard connectors, the PCBs ensure compatibility and ease of integration with various external devices. This eliminates the need for custom connectors, which can be time consuming and costly to manufacture. In addition, the availability of standard connectors on the market means that replacements can be easily sourced in the event of damage or failure. Overall, the use of standard connectors simplifies the assembly process and improves the overall functionality of the PCBs when connecting to external devices.

6.7. PCB Interconnection

To ensure seamless communication and operation, it is essential that all the PCBs in the system are interconnected. This interconnected network allows for the exchange of vital information and coordination between different components, ensuring the smooth operation of the overall system. Proper routing of the interconnections between the PCBs can minimise signal degradation and crosstalk, resulting in reliable and efficient data transfer.

When designing interconnects, various routing techniques are used to maximise performance and minimise any negative effects. One widely used technique is the use of differential signalling, where pairs of conductors carry complementary signals that cancel out any noise and interference.

In addition to the use of differential signalling, other routing techniques such as controlled impedance routing and proper grounding techniques are also used. Controlled impedance routing ensures that the impedance of the signal traces matches the characteristic impedance of the transmission lines, reducing reflections and maintaining signal integrity. Proper grounding techniques help eliminate ground loops and reduce noise, ensuring clean and stable signal transmission.

By incorporating these routing techniques and ensuring proper connections between all PCBs, the system enables seamless communication and increases energy efficiency during operation, which affects overall power consumption (and therefore heat dissipation).

6.8. Electrical Requirements

PCBs shall be designed to operate with DC currents within the specified voltage range to ensure compatibility with associated components and power sources. Power distribution networks are designed to handle the expected currents, taking into account safety margins and avoiding voltage drops.

6.9. Mechanical Considerations

The mechanical design of the printed circuit boards will conform to the target dimensions of the system. PCBs are manufactured using robust materials with appropriate thickness to maintain structural integrity and prevent bending or warping during operation or mechanical stress.

6.10. Conclusion

This part of the report has outlined the specifications for the design and manufacture of the printed circuit boards that will be used in the project. The separate PCBs for heater control, PCM control, lasers and detection structures will be interconnected using standard edge connectors and SMA connectors. The design will focus on electrical performance, thermal management and mechanical stability to ensure optimal functionality and reliability in the intended applications. Board to board interconnectivity will be provided using commonly used and commercially available edge connectors.

7. Technical specifications, conceptual designs and integration process flow of InP lasers and PD

7.1. Design and optimization of the InP – to – SiN interface

In this section, the optimization procedure of the InP-to-SiN interface performed by UOI is presented. An adiabatic coupling scheme was designed and optimized for the efficient light transition from/to InP active (Laser/PD) to/from SiN photonic platform, at 1550 nm for TE polarization. In doing this, a polycrystalline-Si (p-Si) intermediate layer was utilized to bridge the refractive index mismatch between the SiN WG and III-V stack. Specifically, a two-stages taper configuration was optimized to couple the light out of the SiN WG in the p-Si WG and subsequently to a mode that overlaps with the active layer in the III-V stack (i.e. coupling to the Uni-Traveling Carrier Photodiodes - UTC-PD) and vice-versa (i.e. coupling from the Semiconductor Optical Amplifier – SOA/LASER to the SiN photonic WG platform). Designs were fully aligned with the different fabrication processes taking input from the corresponding partner: LGT (SiN, p-Si photonic platform), SMART (InP actives), XCEL (µTP) i.e. refractive indices, layered cross sectional stack, thickness of each layer, critical dimensions of fabrication and tolerances to misalignment error. Here, we present the updated designs of the SOA-to-SiN interface and the designs of the SiN-to-UTC-PD interface, resulting to the optimized specifications in both III-V actives' coupling schemes.

7.2. SOA-to-SiN interface

The optimization procedure of the two-stages tapering (i.e. III-V passive tapering for the transition from SOA to p-Si WG and subsequently the p-Si tapering for the transition from p-Si to SiN WG), was presented in detail in the deliverable D1.1 (Section 4.3, WP3/Task 3.3). There, we explored various parameters in a wide range i.e. WG widths, tapering lengths, p-Si thickness and misalignment tolerances indicated from the different fabrications processes (SMART, LGT, XCEL) resulting in the optimized parameters that lead to 96.2% (-0.17dB) Total Transmission i.e. 98.5 % from SOA to p-Si WG and 97.6 % from p-Si to SiN WG. Also, back reflection to the fundamental TE mode appears far below the level of 50 dB for µTP misalignment errors in the range of 0 – 1 µm. Here, we evaluate the effect of the n-InP thickness increment from 200 nm to 300 nm as it was indicated from SMART because, it was found highly beneficial in terms of fabrication. Thus, in Table 9, we present the Transmission from SOA to p-Si for the two n-InP thicknesses and two p-Si WG widths 3 µm (optimum) and 5 µm (good tolerance to µ-TP misalignment errors). Increasing the n-InP thickness, the Transmission is decreased because of the weaker coupling of the TE-

mode in the III-V passive stack with the TE-mode in the p-Si WG. Thus, it needs longer passive taper lengths to mitigate this effect, i.e. increase the passive taper length from 250 μm (98.5%) to 400 μm (97.1%) to achieve similar Total Transmission from 96.2% (-0.17dB) to 94.7% (-0.23dB) including the transition from p-Si to SiN WG. This passive tapering will be implemented in the SOA/Laser active structures at the 1st fabrication Run in AMBROSIA.

Table 9: Transmission efficiency from SOA to p-Si for the two n-InP thicknesses (200 nm and 300 nm) and two p-Si WG widths (3 μm and 5 μm) at specific passive taper lengths.

L (um)	$W3_{pSi}$ = 3 um		$W3_{pSi}$ = 5 um	
h n-InP	200 nm	300 nm	200 nm	300 nm
250	98.5	92.8	98.7	91.1
300	98.6	95.1	98.6	93.4
350	98.5	96.7	98.5	95.0
400	98.3	97.1	98.6	96.1
450	98.1	97.2	98.5	96.9
500	97.9	97.3	98.3	97.4

7.3. SiN-to-UTC-PD interface

Similarly, for the case of UTC-PD interface, we re-designed the adiabatic coupling scheme for the light transition from SiN WG to p-Si WG and subsequently to UTC-PD for both TE and TM Polarizations. In this case we explored the two polarizations because UTC-PD can be worked in both, as it was indicated by SMART. We found that TM is not applicable for this coupling scheme presenting very low Transmission efficiency i.e. < 7% from SiN WG to p-Si WG and < 0.5% from p-Si WG to UTC-PD. On the other hand, this coupling scheme is applicable for the TE activation of both UTC-PD and SOA/LASER. Thus, the involved partners decided to work both actives at TE and incorporate Polarization rotators at the next runs to convert the TE to TM for the activation of the plasmonic sensors. Subsequently, we present the optimization procedure of the SiN/p-Si/UTC-PD coupling interface at TE polarization. The first stage coupling from SiN to p-Si WG was optimized for TE at the SOA/LASER coupling scheme reaching 97.6% Transmission. In the second stage coupling from p-Si to UTC-PD, the incident fundamental TE-mode from the p-Si WG is adiabatically coupled throughout a III-V passive taper length to the TE-even mode supported at the end of the taper. Subsequently, the TE-even mode is coupled at the III-V passive to UTC-PD active interface to different TE modes supported by the absorbing UTC-PD active stack. The transmitted power ($|t_{1j}|^2$) of the TE-even mode (1) to each mode (j) in UTC-PD active stack is extracted through mode overlap analysis. Each mode is propagating independently in the absorbing active medium stack, where the total Transmission can be calculated as:

$$T = \sum |t_{1j}|^2 e^{-2Im\{\beta_j\}L_{Active}}$$

where $Im\{\beta_j\} = 2\pi Im\{neff_j\}/\lambda$ is the imaginary part of the complex propagation constant of each mode (j) and L_{Active} is the Length of the UTC-PD active stack. While the Total Absorption of light in the UTC-PD active stack is defined as:

$$A = \sum |t_{1j}|^2 \left(1 - e^{-2Im\{\beta_j\}L_{Active}}\right)$$

To optimize the light detection of the UTC-PD, we need to maximize the Transmission from the p-Si WG to the III-V passive taper by tuning the taper length and the subsequent Absorption in the UTC-PD active stack by tuning the active length. For the optimized taper length of 400 µm the Transmission from the p-Si WG to the III-V passive is reaching to 98.7% (3 µm p-Si WG width). Considering the transition from SiN to p-Si WG the Total Transmission drops to 96.3 %, as it is summarized in Table 10 (a). This passive tapering will be implemented in the UTC-PD active structures at the 1st fabrication Run in AMBROSIA. Subsequently, the TE-even mode is coupled at the passive to active interface at the TE modes supported by the absorbing UTC-PD active stack. Depending on the propagation constant of each mode some of these modes are totally absorbed in the 25 µm of the UTC-PD active stack while others are not absorbed, leaving 37% of coupling light unabsorbed. Note that this light could be absorbed in the extreme active length > 1 mm. Finally, in Table 10 (b) we present the total Absorption of the UTC-PD considering all the transitions from SiN to active stack, reaching to 58.2 % (37 % unabsorbed) and 38.8 % (56 % unabsorbed) Total Absorption for p-Si widths 3 µm and 5 µm, respectively. One way for the further optimization of UTC-PD coupling, is to redesign the UTC-PD stack (layer thicknesses and width) with respect to fabrication restrictions, in order to increase the coupling to highly absorbing modes.

Table 10: (a) Total Transmission at the end of the passive tapering calculated as the Transmission from SiN to p-Si WG times the Transmission from p-Si to III-V passive (b) Total Absorption in the first 25 µm of Active Length assuming the transition from 400 µm Passive Taper Length of (a).

(a)

III-V Passive	Trans. from SiN to Passive (%)	
Taper Length (um)	$W3_{pSi}$ = 3 um	$W3_{pSi}$ = 5 um
400	96.3	95

(b)

UTC-PD Active	Total Abs. for $L_{passive}$ = 400 µm (%)	
Length (um)	$W3_{pSi}$ = 3 um	$W3_{pSi}$ = 5 um
25	58.2	38.8

7.4. Micro-transfer printing (µTP) Specifications

As part of task 2.1, the specifications for integration of the III-V device and receiving substrate design must be optimized to ensure µTP can be successfully carried out.

The µTP tool uses image recognition software to align the III-V device to the receiving substrate. This software will search for a pre-defined pattern on the laser coupon and PIC surface in order to measure and adjust the X,Y offset prior to printing. Metal alignment marks are preferred as patterns due to their high reflectivity and contrast. For scenarios where metal layers need to be avoided and cannot be used in either the source chiplets or the target wafers, other materials can also be used as alignment such as photoresists, dielectrics, etched/topography features. For WP3 the alignment feature on the PIC substrate will be defined during the etch into the polysilicon layer while the laser will have metal alignment features at both end of the coupon.

In addition, alignment features on the coupon and PIC must be within FOV (490x370um) of the camera used by the µTP tool. The minimum line width of an alignment feature should be ~7um so the image recognition software can detect the position accurately. Alignment feature templates used successfully in previous work were presented to WP3 partners (see Figure 10).

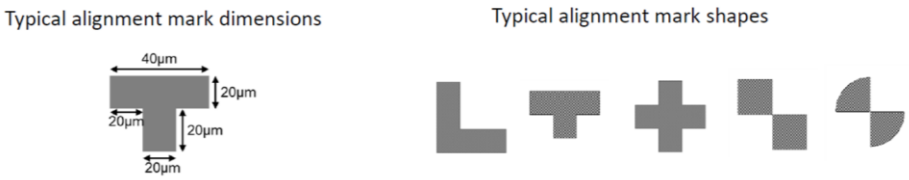

Figure 10. µTP alignment mark templates.

To avoid distortion of the image and shadowing that may result unreliable alignment patterns we specify the following:

- the PIC alignment features should be a distance of 35µm from the III-V device,
- the alignment features on the III-V coupon must be 5µm from the edge of the coupon,
- the III-V device must be 20µm from the edge of the cavity

7.5. µTP Process Flow

As part of Task 2.2, XCEL will define the process flow for the Micro-transfer printing (µTP) process (Figure 11). µTP will be utilized to integrate the III-V devices onto the SiN platform and uses a PDMS stamp to pick and print singulated micro-structures to a receiving substrate. Image recognition software is used to accurately align the coupon to within the required tolerances.

XCEL will receive the SiN wafer from LGT as well as µTP-compatible III-V wafers from SMART. Within Task 3.3 a series of sub-tasks will be undertaken to integrate the III-V devices on the SiN PIC and form electrical connections for testing. First, 30nm BCB is spray coated onto the SiN wafer to ensure good bonding strength and print yield. µTP is used to integrate the III-V devices onto the SiN wafer with an accuracy of 0.5-1um as defined by UOI and any exposed BCB is removed with an F-based O2 etch. The contact pad and circuit formation will be undertaken by a subcontractor using electroplating of either Au or Cu. The final step is to apply a SiO_2 passivation layer to the wafer and open contact pads by etching the SiO_2. Following these assembly steps, the wafer will be singulated into chips at LGT before being tested at chip level at AUTH.

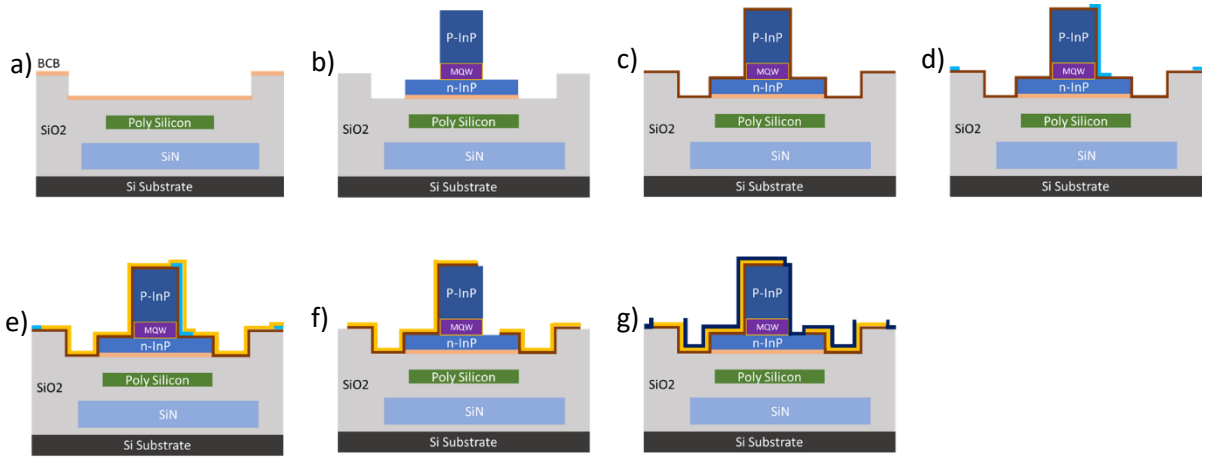

Figure 11. Process flow for MTP steps: a) adhesive coat, b) MTP, c) seed layer deposition, d) pattern photo-resist, e) electroplating, f) resist lift off, g) passivation.

SMART PHOTONICS will provide µ-transfer printable coupons of active photodetectors (PDs) and semiconductor optical amplifiers (SOAs). The specifications of the µ-transfer printable coupons of PDs and SOAs gain blocks can be found in Table 11 and Table 12, respectively. The specifications are not fully determined because the components are under development, however the specification table will be complete as soon as the manufacturing & characterization steps be done. Further details about the PDs and SOAs are discussed further in the text.

Table 11. PD specifications for the 1st run.

BB	Parameters	Target specs	1st run specs	2nd run specs
	Photodiode type	UTC	UTC	UTC
C-band PD	Dark current	20 nA	t.b.d.	20 nA
	Responsivity	0.8 A/W	t.b.d.	0.8 A/W
	Sensitivity	<-50 dBm	t.b.d.	<-50 dBm
	Coupling losses	1.5 dB	t.b.d.	1.5 dB
	Footprint	t.b.d.	t.b.d.	t.b.d.
	Mode	TM	TM	TM

Table 12. SOA specifications for the 1st run.

BB	Parameters	Target specs	1st run specs	2nd run specs
	Laser type	To be determined	Hybrid	t.b.d.
C-band laser	Wavelength band/range	1550 ± 40 nm	1550 nm	1550 ± 40 nm
	Linewidth	≅100 kHz	t.b.d.	≅100 kHz
	Footprint (max)	0.7x2 mm^2	0.05x2.22-2.73 mm^2	t.b.d.
	Output power	10 dBm	10 dBm	10 dBm
	Temperature operating range	RT	RT	RT
	Power consumption	100 mW	t.b.d.	100 mW
	Mode	TE	TE	TE

8. Technical specifications, conceptual designs and integration process flow of microfluidics

MLIQ has prepared the microfluidics chip design taking input for the required specifications from other related partners (AUTH, LGT, ICN2, ARGO). The complete sensor chip will have a size of 22 x 17 mm^2 (specifically 21.88 x 16.91 mm2), of which 22 x 15.5 mm^2 will be available for the microfluidics. The remaining 1.5 x 22 mm^2 will be reserved for the PCB connection as agreed with ARGO. Due to the overall dimensions of the chip and to ensure enough space between the channels (at least 1.65 mm), the microfluidics chip will have 8 channels, these channels shall have a length of 14 mm and a width of 250 microns.

This will mainly help the sealing, increasing the contact surface between the PDMS and the chip. This sealing will be done mechanically by means of a PMMA holder, allowing the assembly to be disassembled for cleaning and reuse. Additionally, it has been decided to use inlets and outlets for each of the channels in order to enable the measurement of different indicators and to facilitate the functionalization of the different channels. Also, the outlets allow the waste products to be removed from the process. These connections will be made by means of 1/16" tubing directly into the fluidic orifices.

9. Preliminary specifications of PoC platforms. Readout subsystem

The PoC Platform will have a portable size, 30cm×15cm×20cm (L×W×H), while the mass should be considered as ideal if it weighs less than 2 kg. The aforementioned physical parameters will depend on the final arrangement of the subsystems, thus these two are subjects to change. The system will read out the signals coming from the various electronic boards and translate them into meaningful indications related to positive or negative detection of the sepsis condition. Our target is to operate the platform with a minimum power (ideally 5-15W). However, this depends strongly on the power requirements of the laser, if we will use a screen integrated with the system, and the capacity needed for the algorithms to perform their calculations. Thus, this is another potential subject to change. We will use either IDE Arduino or Python as the language of programming. One of the critical components is the readout electronics board, as this will be designed in house, and depends strongly on the layout and operation of the plasmo-photonic chip and neurochip. The design of the PoC is the one presented in Figure 12.

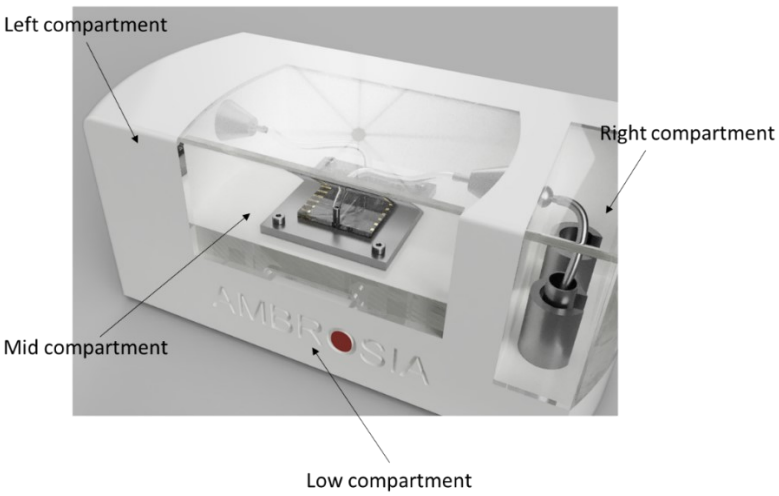

Figure 12. AMBROSIA's PoC Platform.

The PoC platform will consist of different compartments (as shown in Figure 12), where all the electronic boards, pumps, laser modules and neurochip will be placed. The design will be in an industrial level, in order to easily replace any of the components. The mid compartment will have a special slot where the plasmo-photonic chip will be placed, ensuring an electrical connection with the platform. On top of the chip, the microfluidics module will handle the delivery of any solution on its surface, by pumping liquid from the right compartment, where the user will be able to position vials, containing the sample for analysis (see Figure 13). A micro-pump will be located in the left-compartment, ensuring the continuous flow, towards the detection chip.

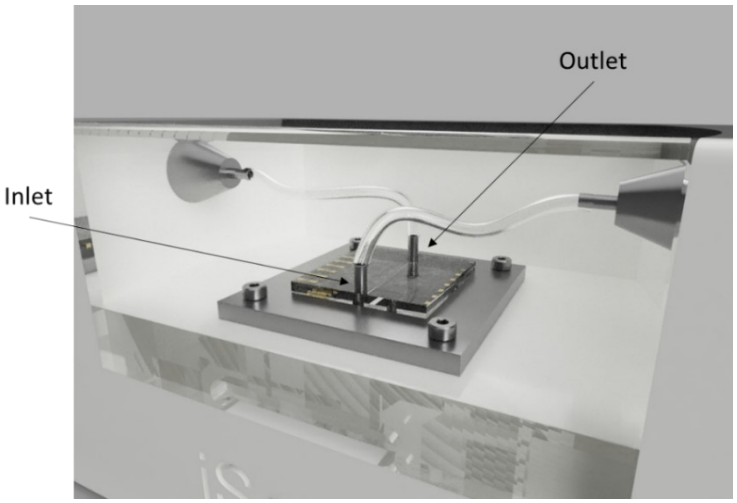

Figure 13. Compartment that hosts the plasmo-photonic and microfluidic chips.

10. Conclusions

This deliverable outlines the preliminary details associated with the development of the AMBROSIA prototypes. It encompasses various aspects, including the preliminary list of sepsis biomarkers for the set-up of the AMBROSIA diagnostic system, the architectural and conceptual design of the device, as well as the specifications and usage scenarios for diagnosing sepsis in clinical settings.

A preliminary list of sepsis biomarkers for the set-up of the AMBROSIA diagnostic system has been made taking into account how their measure can contribute to the following areas: (I) early detection of sepsis in patients displaying systemic inflammatory response syndrome (SIRS); (II) risk stratification and prognosis evaluation of septic patients; and (III) guiding and monitoring antibiotic therapy in various sepsis scenarios. For this purpose, the selected sepsis biomarkers are the following: c-reactive protein (CRP), procalcitonin (PCT), interleukin-6 (IL-6), mid-regional fragment of pro-adrenomedullin (MR-proADM). In addition, taking into account the technical possibilities of the AMBROSIA biosensor prototype, the detection of the following bacterial will be considered: *Escherichia coli, Staphylococcus aureus* and *Pseudomonas aeruginosa.* The range of concentrations to be detected for each biomarker have also been specified according to their relevant levels in clinical diagnostics.

Finally, a description of the technical aspects required for the different components (sensor chips, microfluidics and electronics) design, fabrication and integration is provided. This includes detailed information of each step individually and a general view of the initial requirements for the portable PoC

version of the AMBROSIA biosensing platform, including details on the readout subsystem. The information on these technical aspects may be updated and refined as the project progresses.

11. References

1. Rudd KE, Johnson SC, Agesa KM, Shackelford KA, Tsoi D, Kievlan DR, Colombara DV, Ikuta KS, Kissoon N, Finfer S, Fleischmann-Struzek C, Machado FR, Reinhart KK, Rowan K, Seymour CW, Watson RS, West TE, Marinho F, Hay SI, Lozano R, Lopez AD, Angus DC, Murray CJL, Naghavi M. Global, regional, and national sepsis incidence and mortality, 1990-2017: analysis for the Global Burden of Disease Study. Lancet. 18 de enero de 2020;395(10219):200-11.

2. Fleischmann C, Scherag A, Adhikari NKJ, Hartog CS, Tsaganos T, Schlattmann P, Angus DC, Reinhart K, International Forum of Acute Care Trialists. Assessment of Global Incidence and Mortality of Hospital-treated Sepsis. Current Estimates and Limitations. Am J Respir Crit Care Med. 1 de febrero de 2016;193(3):259-72.

3. Singer M, Deutschman CS, Seymour CW, Shankar-Hari M, Annane D, Bauer M, Bellomo R, Bernard GR, Chiche JD, Coopersmith CM, Hotchkiss RS, Levy MM, Marshall JC, Martin GS, Opal SM, Rubenfeld GD, van der Poll T, Vincent JL, Angus DC. The Third International Consensus Definitions for Sepsis and Septic Shock (Sepsis-3). JAMA. 23 de febrero de 2016;315(8):801-10.

4. Baldirà J, Ruiz-Rodríguez JC, Wilson DC, Ruiz-Sanmartin A, Cortes A, Chiscano L, Ferrer-Costa R, Comas I, Larrosa N, Fàbrega A, González-López JJ, Ferrer R. Biomarkers and clinical scores to aid the identification of disease severity and intensive care requirement following activation of an in-hospital sepsis code. Ann Intensive Care. diciembre de 2020;10(1):7.

5. Jones AE, Trzeciak S, Kline JA. The Sequential Organ Failure Assessment score for predicting outcome in patients with severe sepsis and evidence of hypoperfusion at the time of emergency department presentation. Crit Care Med. mayo de 2009;37(5):1649-54.

6. Vincent JL, de Mendonça A, Cantraine F, Moreno R, Takala J, Suter PM, Sprung CL, Colardyn F, Blecher S. Use of the SOFA score to assess the incidence of organ dysfunction/failure in intensive care units: results of a multicenter, prospective study. Working group on «sepsis-related problems» of the European Society of Intensive Care Medicine. Crit Care Med. noviembre de 1998;26(11):1793-800.

7. Spoto S, Nobile E, Carnà EPR, Fogolari M, Caputo D, De Florio L, Valeriani E, Benvenuto D, Costantino S, Ciccozzi M, Angeletti S. Best diagnostic accuracy of sepsis combining SIRS criteria or qSOFA score with Procalcitonin and Mid-Regional pro-Adrenomedullin outside ICU. Sci Rep. 6 de octubre de 2020;10(1):16605.

8. Improving knowledge about sepsis 3 definition in critically ill patients: new insights - Martínez - Journal of Emergency and Critical Care Medicine [Internet]. [citado 25 de julio de 2023]. Disponible en: https://jeccm.amegroups.org/article/view/4290/html

9. Lambden S, Laterre PF, Levy MM, Francois B. The SOFA score-development, utility and challenges of accurate assessment in clinical trials. Crit Care. 27 de noviembre de 2019;23(1):374.

10. Ferreira FL, Bota DP, Bross A, Mélot C, Vincent JL. Serial evaluation of the SOFA score to predict outcome in critically ill patients. JAMA. 10 de octubre de 2001;286(14):1754-8.

11. Schuurman AR, Sloot PMA, Wiersinga WJ, Van Der Poll T. Embracing complexity in sepsis. Crit Care. 11 de marzo de 2023;27(1):102.

12. Meynaar IA, Droog W, Batstra M, Vreede R, Herbrink P. In Critically Ill Patients, Serum Procalcitonin Is More Useful in Differentiating between Sepsis and SIRS than CRP, Il-6, or LBP. Crit Care Res Pract. 2011;2011:594645.

13. Sierra R, Rello J, Bail&#65533;n MA, Ben&#65533;tez E, Gordillo A, Le&#65533;n C, Pedraza S. C-reactive protein used as an early indicator of infection in patients with systemic inflammatory response syndrome. Intensive Care Medicine. noviembre de 2004;30(11):2038-45.

14. Simon L, Gauvin F, Amre DK, Saint-Louis P, Lacroix J. Serum procalcitonin and C-reactive protein levels as markers of bacterial infection: a systematic review and meta-analysis. Clin Infect Dis. 15 de julio de 2004;39(2):206-17.

15. Póvoa P, Coelho L, Almeida E, Fernandes A, Mealha R, Moreira P, Sabino H. C-reactive protein as a marker of infection in critically ill patients. Clin Microbiol Infect. febrero de 2005;11(2):101-8.

16. Póvoa P, Coelho L, Almeida E, Fernandes A, Mealha R, Moreira P, Sabino H. Early identification of intensive care unit-acquired infections with daily monitoring of C-reactive protein: a prospective observational study. Crit Care. 2006;10(2):R63.

17. Lobo SMA, Lobo FRM, Bota DP, Lopes-Ferreira F, Soliman HM, Mélot C, Vincent JL. C-reactive protein levels correlate with mortality and organ failure in critically ill patients. Chest. junio de 2003;123(6):2043-9.

18. Tschaikowsky K, Hedwig-Geissing M, Schmidt J, Braun GG. Lipopolysaccharide-binding protein for monitoring of postoperative sepsis: complemental to C-reactive protein or redundant? PLoS ONE. 2011;6(8):e23615.

19. Tschaikowsky K, Hedwig-Geissing M, Braun GG, Radespiel-Troeger M. Predictive value of procalcitonin, interleukin-6, and C-reactive protein for survival in postoperative patients with severe sepsis. J Crit Care. febrero de 2011;26(1):54-64.

20. Schmit X, Vincent JL. The time course of blood C-reactive protein concentrations in relation to the response to initial antimicrobial therapy in patients with sepsis. Infection. junio de 2008;36(3):213-9.

21. Wacker C, Prkno A, Brunkhorst FM, Schlattmann P. Procalcitonin as a diagnostic marker for sepsis: a systematic review and meta-analysis. The Lancet infectious diseases. 2013;13(5):426-35.

22. Brodská H, Malíčková K, Adámková V, Benáková H, Šťastná MM, Zima T. Significantly higher procalcitonin levels could differentiate Gram-negative sepsis from Gram-positive and fungal sepsis. Clin Exp Med. agosto de 2013;13(3):165-70.

23. Charles PE, Ladoire S, Aho S, Quenot JP, Doise JM, Prin S, Olsson NO, Blettery B. Serum procalcitonin elevation in critically ill patients at the onset of bacteremia caused by either Gram negative or Gram positive bacteria. BMC Infect Dis. 2008;8:38.

24. Reinhart K, Meisner M. Biomarkers in the Critically Ill Patient: Procalcitonin. Critical Care Clinics. abril de 2011;27(2):253-63.

25. Giamarellos-Bourboulis EJ, Tsangaris I, Kanni T, Mouktaroudi M, Pantelidou I, Adamis G, Atmatzidis S, Chrisofos M, Evangelopoulou V, Frantzeskaki F, Giannopoulos P, Giannikopoulos G, Gialvalis D, Gourgoulis GM, Kotzampassi K, Katsifa K, Kofinas G, Kontopidou F, Koratzanis G, Koulouras V, Koutsikou A, Koupetori M, Kritselis I, Leonidou L, Mega A, Mylona V, Nikolaou H, Orfanos S, Panagopoulos P, Paramythiotou E, Papadopoulos A, Papanikolaou X, Pavlaki M, Polychronopoulos V, Skoutelis A, Theodotou A, Vassiliaghou M, Douzinas EE, Gogos C, Armaganidis A, Hellenic Sepsis Study Group. Procalcitonin as an early indicator of outcome in sepsis: a prospective observational study. J Hosp Infect. enero de 2011;77(1):58-63.

26. Bouadma L, Luyt CE, Tubach F, Cracco C, Alvarez A, Schwebel C, Schortgen F, Lasocki S, Veber B, Dehoux M, Bernard M, Pasquet B, Régnier B, Brun-Buisson C, Chastre J, Wolff M. Use of procalcitonin to reduce patients' exposure to antibiotics in intensive care units (PRORATA trial): a multicentre randomised controlled trial. The Lancet. 12 de febrero de 2010;375(9713):463-74.

27. Rodríguez-Gaspar M, Santolaria F, Jarque-López A, González-Reimers E, Milena A, de la Vega MJ, Rodríguez-Rodríguez E, Gómez-Sirvent JL. Prognostic value of cytokines in SIRS general medical patients. Cytokine. 21 de agosto de 2001;15(4):232-6.

28. Billeter A, Turina M, Seifert B, Mica L, Stocker R, Keel M. Early serum procalcitonin, interleukin-6, and 24-hour lactate clearance: useful indicators of septic infections in severely traumatized patients. World J Surg. marzo de 2009;33(3):558-66.

29. Harbarth S, Holeckova K, Froidevaux C, Pittet D, Ricou B, Grau GE, Vadas L, Pugin J, Geneva Sepsis Network. Diagnostic value of procalcitonin, interleukin-6, and interleukin-8 in critically ill patients admitted with suspected sepsis. Am J Respir Crit Care Med. 1 de agosto de 2001;164(3):396-402.

30. Oberhoffer M, Russwurm S, Bredle D, Chatzinicolaou K, Reinhart K. Discriminative power of inflammatory markers for prediction of tumor necrosis factor-alpha and interleukin-6 in ICU patients with systemic inflammatory response syndrome (SIRS) or sepsis at arbitrary time points. Intensive Care Med. marzo de 2000;26 Suppl 2:S170-174.

31. Sakr Y, Burgett U, Nacul FE, Reinhart K, Brunkhorst F. Lipopolysaccharide binding protein in a surgical intensive care unit: a marker of sepsis? Crit Care Med. julio de 2008;36(7):2014-22.

32. Dimopoulou I, Orfanos S, Kotanidou A, Livaditi O, Giamarellos-Bourboulis E, Athanasiou C, Korovesi I, Sotiropoulou C, Kopterides P, Ilias I, Kanellakopoulou K, Armaganidis A. Plasma pro- and anti-inflammatory cytokine levels and outcome prediction in unselected critically ill patients. Cytokine. marzo de 2008;41(3):263-7.

33. Jekarl DW, Lee SY, Lee J, Park YJ, Kim Y, Park JH, Wee JH, Choi SP. Procalcitonin as a diagnostic marker and IL-6 as a prognostic marker for sepsis. Diagn Microbiol Infect Dis. abril de 2013;75(4):342-7.

34. Christ-Crain M, Morgenthaler NG, Struck J, Harbarth S, Bergmann A, Muller B, others. Mid-regional pro-adrenomedullin as a prognostic marker in sepsis: an observational study. Crit Care. 2005;9(6):R816-24.